

Northumbria Research Link

Citation: Wang, Dongyang, Yang, Biao, Gao, Wenlong, Jia, Hongwei, Yang, Quanlong, Chen, Xieyu, Wei, Minggui, Liu, Changxu, Navarro-Cía, Miguel, Han, Jiaguang, Zhang, Weili and Zhang, Shuang (2019) Photonic Weyl points due to broken time-reversal symmetry in magnetized semiconductor. Nature Physics, 15 (11). pp. 1150-1155. ISSN 1745-2473

Published by: Nature Publishing

URL: <https://doi.org/10.1038/s41567-019-0612-7> <<https://doi.org/10.1038/s41567-019-0612-7>>

This version was downloaded from Northumbria Research Link:
<http://nrl.northumbria.ac.uk/id/eprint/47156/>

Northumbria University has developed Northumbria Research Link (NRL) to enable users to access the University's research output. Copyright © and moral rights for items on NRL are retained by the individual author(s) and/or other copyright owners. Single copies of full items can be reproduced, displayed or performed, and given to third parties in any format or medium for personal research or study, educational, or not-for-profit purposes without prior permission or charge, provided the authors, title and full bibliographic details are given, as well as a hyperlink and/or URL to the original metadata page. The content must not be changed in any way. Full items must not be sold commercially in any format or medium without formal permission of the copyright holder. The full policy is available online: <http://nrl.northumbria.ac.uk/policies.html>

This document may differ from the final, published version of the research and has been made available online in accordance with publisher policies. To read and/or cite from the published version of the research, please visit the publisher's website (a subscription may be required.)



**Northumbria
University**
NEWCASTLE



UniversityLibrary

Photonic Weyl points due to broken time-reversal symmetry in magnetized semiconductor

Dongyang Wang^{1,2†}, Biao Yang^{2,3†}, Wenlong Gao², Hongwei Jia², Quanlong Yang¹, Xieyu Chen¹, Minggui Wei¹,
Changxu Liu², Miguel Navarro-Cía², Jianguang Han^{1*}, Weili Zhang^{1,4*}, Shuang Zhang^{2*}

1. Center for Terahertz Waves and College of Precision Instrument and Optoelectronics Engineering, Tianjin University and the Key Laboratory of Optoelectronics Information and Technology (Ministry of Education), Tianjin 300072, China.
2. School of Physics & Astronomy, University of Birmingham, Birmingham, B15 2TT, UK
3. College of Advanced Interdisciplinary Studies, National University of Defense Technology, Changsha 410073, China.
4. School of Electrical and Computer Engineering, Oklahoma State University, Stillwater, Oklahoma 74078, USA

*Correspondence to: jiaghan@tju.edu.cn; weili.zhang@okstate.edu; s.zhang@bham.ac.uk

†These authors contributed equally to this work.

Weyl points are discrete locations in the three-dimensional momentum space where two bands cross linearly with each other. They serve as the monopoles of Berry curvature in the momentum space, and their existence requires breaking of either time-reversal or inversion symmetry¹⁻¹⁶. Although various non-centrosymmetric Weyl systems have been reported¹⁵, demonstration of Weyl degeneracies due to breaking of the time reversal symmetry remains scarce and is limited to electronic systems^{17,18}. Here, we report the experimental observation of photonic Weyl degeneracies in a magnetized semiconductor - InSb, which behaves as magnetized plasma¹⁹ for electromagnetic waves at the terahertz band. By varying the magnetic field strength, Weyl points and the corresponding photonic Fermi-arcs have been demonstrated.

Our observation establishes magnetized semiconductors as a reconfigurable²⁰ terahertz Weyl system, which may prompt research on novel magnetic topological phenomena such as chiral Majorana type edge states and zero modes in classic systems^{21,22}.

Weyl points as topologically chiral singularity points in the three-dimensional momentum space have been extensively investigated in both quantum and classical systems¹⁵. In photonics, Weyl points have been observed in various systems such as gyroid photonic crystals^{7,23}, metamaterials²⁴⁻²⁶, and evanescently coupled helical waveguides²⁷. However, all the previously demonstrated photonic Weyl points are exclusively based on systems with broken inversion symmetry¹⁵. On the other hand, it has been proposed that Weyl points due to breaking of the time-reversal symmetry may possess more interesting properties such as axial anomaly, giant photocurrent and novel quantum oscillation phenomena²⁸⁻³⁰. They may enable multiple striking topological features such as Majorana type edge states and zero mode²², which do not exist in inversion symmetry breaking systems. Although there have been theoretical proposals on implementation of Weyl degeneracies by applying external magnetic fields on finely designed photonic crystals^{16,31}, very few of them are easily realizable in experiment due to the challenge in three-dimensional structuring of magnetic materials^{32,33}. Interestingly, it was recently theoretically proposed that plasma, the fourth fundamental state of natural matter^{34,35}, can support Weyl degeneracies under external magnetic fields¹⁹, as well as nonreciprocal wave transport³⁶⁻³⁸. Since there is no structuring involved, this represents a facile and tunable approach for achieving photonic Weyl degeneracies arising from time-reversal symmetry breaking.

In this work, by applying magnetic field to intrinsic semiconductor InSb, we demonstrate photonic Weyl points due to broken time reversal symmetry. Here InSb^{39,40} is chosen because of its very small effective mass of electrons ($m^* = 0.015m_0$, where m_0 is the free electron mass) that can lead to a terahertz cyclotron frequency under a moderate applied magnetic field. Along the direction of magnetic field, electrons can move freely. Therefore, the dielectric function is described by the Drude model, and there exists a longitudinal bulk plasma mode along the applied magnetic field. However, in the plane perpendicular to the magnetic field, the dielectric function is significantly modified due to

the cyclotron motion of electrons, which leads to the breaking of degeneracy between the left and right circular polarizing (L/RCP) modes propagating along the magnetic field^{40,36}. The linear crossing between the longitudinal plasma mode and a circular polarizing mode forms a Weyl point in the magnetized plasma system¹⁹. By considering the coupling between the electromagnetic wave and the motion of the free charges in the plasma, we can derive a full Hamiltonian H as (see supplementary information 1)¹⁹:

$$\omega_p \begin{bmatrix} 0 & -k \times / \sqrt{\epsilon_\infty} k_p & -i / \sqrt{\epsilon_\infty} \\ k \times / \sqrt{\epsilon_\infty} k_p & 0 & 0 \\ i \sqrt{\epsilon_\infty} & 0 & (\omega_c \Delta - i \gamma I) / \omega_p \end{bmatrix} \begin{bmatrix} E \\ H \\ V \end{bmatrix} = \omega \begin{bmatrix} E \\ H \\ V \end{bmatrix} \quad (1)$$

where $\omega_p = \sqrt{ne^2 / \epsilon_0 \epsilon_\infty m^*}$ and $\omega_c = eB / m^*$ are the plasma frequency and electron cyclotron frequency, respectively, with n being the free electron density, ϵ_0 the permittivity of vacuum and $\epsilon_\infty = 16$ the dielectric constant at high frequencies; k_p is the vacuum wave vector at the plasma frequency, γ is the damping frequency and $\Delta = [\sigma_y, 0; 0, 0]$ with σ_y being the second Pauli matrix. By carefully controlling the temperature, the carrier density of InSb can be tuned to give a plasma frequency around $\omega_p / 2\pi = 0.3$ THz, which falls in the frequency range of our terahertz measurement setup. Depending on the relative values of ω_c and ω_p , different numbers of Weyl points may show up in our system (see supplementary information 2, Fig. S1). When $\omega_c > \omega_p$, there are two pairs of Weyl points appearing at the plasma frequency with the momentum coordinates $(k_x, k_y, k_z) = (0, 0, \pm \sqrt{\epsilon_\infty \omega_c / (\omega_c \pm \omega_p)})$, where the magnetic field is applied along z direction. Around the outer Weyl point (located at larger k_z), the first order $k \cdot p$ Hamiltonian expansion can be expressed as:

$$H_1 = \frac{N}{2} (\sigma_0 + \sigma_3) (M \delta k_z + \xi P \delta B) + N \sigma_1 \delta k_y - N \sigma_2 \delta k_x \quad (2)$$

with parameters M, N, P being linear dispersion coefficients defined by the coordinates at the outer Weyl point, ξ the cyclotron constant and σ_i the Pauli matrices as described in supplementary information 3.

For a semiconductor InSb under a magnetic field strength of $B = 0.19$ T, the corresponding cyclotron frequency is $\omega_c / 2\pi \approx 0.35$ THz, which leads to the band structure shown in Fig. 1a, where plasma frequency is taken as $\omega_p / 2\pi = 0.31$ THz. Along the magnetic field, four double degenerate Weyl points

are located at the plasma frequency as expected. Here, we only consider the outer pair of Weyl points as the inner pair with opposite topological charges are enclosed by the same equifrequency surface and therefore they are not responsible for the observed topological features. Fig. 1b shows the projected band structure around one of the outer Weyl points. It is shown that the dispersions of two participating modes divide the momentum-energy space into four regions representing the bulk states and gaps, respectively. This projected band morphology as a signature of photonic Weyl points can be observed through the reflection spectra when scanning the wave vector k_z . However, in the experiment, scanning k_z requires an angle resolved reflection system, which is incompatible with our magnetic terahertz system. Equivalently, we can scan the magnetic field strength B instead of k_z , since they behave similarly in constructing the parameter space of the Weyl point, as shown by the form of effective Hamiltonian in Eq. 2. Fig. 1c shows the band structure constructed in the synthetic parameter space $[k_x, k_y, B]$ for a fixed incident wave vector of $k_z = 2\pi/90 \text{ } \mu\text{m}^{-1}$. One can see that the linear crossing is preserved in the substituted band structure (Fig. 1d, e), confirming the presence of Weyl points in the synthetic parameter space (for detailed proof, see supplementary information 3).

In order to characterize the Weyl point, we apply a magnetic field along an in-plane direction (parallel to the surface), as shown in Fig. 2a. It is expected that two Weyl points of opposite chiralities appear along the direction of B field. They are both located outside the light cone. In order to probe the reflection spectra around the Weyl points, we employ a grating to compensate the in-plane momentum mismatch between the incident terahertz wave and the Weyl points. The aluminum grating, fabricated directly on the surface of the InSb wafer, has a period of $p = 90 \text{ } \mu\text{m}$, a filling ratio of $2/3$ and a thickness of $t = 1 \text{ } \mu\text{m}$. The sample is then placed in a low temperature environment of $T = 50 \text{ K}$ to provide a plasma frequency of $\omega_p/2\pi \approx 0.31 \text{ THz}$ with a damping factor of $\gamma/2\pi = 3 \times 10^{10} \text{ Hz}$. A normal incidence configuration is employed with the magnetic field applied along the grating direction, as shown in Fig. 2b. A high resistivity float zone Silicon 50/50 terahertz beam splitter is used for the reflection spectra measurement (refer to Methods). The grating provides a fundamental order wave vector of magnitude $G = 2\pi/p$ to excite both the bulk and surface states supported by the magnetized InSb. As the magnetic field strength is scanned from 0-1 Tesla, we measure the reflection spectrum. These measurements

provide the projected band information as shown in Fig. 2c, where the band crossing can be clearly observed at the frequency of $\omega_p/2\pi = 0.31$ THz and magnetic field of $B = 0.19$ T. Fig. 2d shows the corresponding full wave simulation results that take into account the actual dissipation in the magnetized plasma. Simulation results shown in Fig. 2d show good agreement with the experimental results. On the other hand, when the grating direction is rotated away from the direction of magnetic field, the crossing point disappears and a bandgap is formed, as shown in supplementary information 4, Fig. S2. The experimental results confirm the presence of Weyl degeneracies in a magnetized semiconductor system.

The most important signature of a Weyl system is the presence of Fermi-arcs. The photonic Fermi-arcs in the original momentum space are explored in the supplementary information 5 where the surface states are found to be separated into two separated frequency bands: $\omega < \omega_p$ and $\omega > \sqrt{\omega_p^2 + \omega_c^2}$ with opposite signs of k_y , respectively, due to the magnetic field induced cyclotron resonance. These two branches of surface states are observed in the experimentally measured f - B plot manifested as absorption lines in the reflection spectra. The theoretically calculated surface states are indicated by a black dashed line in both the experimental and simulated results in Fig. 2c-d, which fits well with the corresponding surface states induced absorption.

To further explore the surface state features in the magnetized Weyl system, a second experimental configuration is employed as shown in Fig. 3a, in which the incidence terahertz beam and the applied magnetic field are arranged to form angles $\theta = 45^\circ$ and $\alpha = 45^\circ$ with respect to the sample normal and sample surface, respectively. In this configuration, a beam splitter is not required and therefore the signal noise ratio of the measurement is improved by approximately four times in comparison to that of normal incidence. Rotating the grating around x axis by an angle of φ as shown in Fig. 3a (bottom-left inset) provides a non-zero k_y to excite the off k_z axis surface states on the k_y - k_z plane, as shown in Fig. 3a (right insets). Meanwhile, due to the tilted incidence, the degeneracy between $\pm 1^{\text{st}}$ grating order is lifted. The $\pm 1^{\text{st}}$ order excitation wave vector is given by $[k_y, k_z]_{\pm 1} = [\pm G \sin\varphi, \pm G \cos\varphi + k_0 \sin 45^\circ]$ as illustrated in Fig. 3a (bottom-left inset), where φ is the angle formed between the grating momentum

and z axis. For a given magnetic field, it is expected that the $\pm 1^{\text{st}}$ order with opposite signs of k_y can excite surface states at the two aforementioned frequency bands (see supplementary information 5, Fig S3).

In this tilted configuration, the Weyl points are projected onto the sample surface with a smaller in-plane wave vector ($k_z = \pm \sqrt{\epsilon_\infty \omega_c / 2(\omega_c - \omega_p)}$), as shown in Fig. 3b. A different sample with a greater grating periodicity of $p = 120 \text{ } \mu\text{m}$ is therefore designed to match the momentum. The new sample has a similar plasma frequency $\omega_p / 2\pi \approx 0.31 \text{ THz}$ as the previous one. The projected bulk bands on $B - f$ plane are plotted for $\varphi = -30^\circ$ and -45° in Fig. 3c and f, where the bulk states excited by the $\pm 1^{\text{st}}$ grating orders have a large overlap with each other and are indicated by navy and purple color, respectively. The surface states excited by the $\pm 1^{\text{st}}$ grating orders are also calculated and shown in Fig. 3c and f, respectively. At each grating angle φ , the $\pm 1^{\text{st}}$ order excitations with opposite signs of k_y form two separate branches, which merge into each other at zero applied magnetic field B . It is also observed that at increasing φ , the angle between two surface state branches widens, due to the increase in the slopes of the dispersion. It can be noticed that the surface state is interrupted around the cyclotron position, which is caused by the strong cyclotron resonance that leads to relatively high reflection⁴¹. For a negative φ , the diffraction orders that excite the two surface state branches switch in comparison to that with a positive φ (see more discussion in supplementary information 6, Fig. S4).

The measured reflection spectra are shown in Fig. 3e and Fig. 3h for $\varphi = -30^\circ$ and -45° (see supplementary information 7, Fig. S5 for more measured results), respectively, which presents the superposed band projection for both bulk and surface states. The corresponding simulation results for the reflection spectra shown in Fig. 3d and g are in good agreement with the experiment results. It is noticed that there exists a cut-off for the surface state branch at higher frequencies, due to the limited momentum provided by the grating (see supplementary information 8, Fig. S6). Higher grating orders are also excited in the experiment, which contribute to the absorptions along the surface state branch at the higher frequencies beyond the cut-off of the first grating order.

For a given grating diffraction order, the projection of photonic Weyl point can also be described in the parameter space $[\varphi, B]$. Using the same configuration as in Fig. 3a, a sample with higher plasma frequency of $\omega_p/2\pi \approx 0.53$ THz and grating periodicity of $p=150\mu\text{m}$ is measured (supplementary information 9, Fig. S7). The Weyl point which is projected at location $(k_y, k_z) = (0, G + k_0 \sin 45^\circ)$ in the momentum space turns into $(\varphi, B) = (0, 0.472)$ for the +1st grating order (supplementary information 10, Fig. S8). The projected dispersion of the bulk states with respect to B for $\varphi = 0$ is shown in Fig. 4a, where a linear crossing indicating an effective Weyl point is observed. The linear dispersion with respect to φ around the effective Weyl point is confirmed in Fig. 4b. The calculated surface states for different grating orientation angle φ are shown in Fig. 4c and d, where it is clearly shown that larger orientation angles lead to steeper dispersion in B . A photonic Fermi-arc in the B - φ plane can thus be constructed at a given frequency. For the +1st grating order excitation, the photonic Fermi-arcs together with the bulk bands at two different frequencies 0.46 THz and 0.6 THz are shown in Fig. 4e and f, respectively. The experimental data (cyan hollow dots) are in good agreement with the theoretical result. The small deviation between measurements and theory may arise from the nonlocal effect, i.e. spatial dispersion, of the material^{42,43}. It should be noted that due to the presence of loss, the Weyl point transforms into exceptional ring¹⁹, which possesses the same topological charge as a Weyl point. The size of the ring is calculated based on the actual dissipation of the semiconductor and is found to be negligibly small (see supplementary information 11, Fig. S9). Meanwhile, a discussion of the loss and surface wave resonance is shown in supplementary information 12, Fig. S10.

The demonstrated time-reversal breaking Weyl points in magnetized plasma will promote the investigation of topological phases in magnetoplasmon²², where classical chiral Majorana edge states and zero modes have been proposed. Moreover, by introducing spatially variant magnetic field or temperature, synthetic gauge potential can be realized, which may enable observation of other topological exotic effects, such as chiral⁴⁴ and gravitational⁴⁵ anomaly, which are initially investigated in high energy physics and astrophysics. The observed Weyl points and topological surface states in the magnetized InSb also represent the first demonstration of topological phases in the terahertz band, which may facilitate the development of terahertz topological devices.

193

194 **Methods:**

195 The low temperature and high magnetic field environment are provided by a liquid Helium based
196 commercial SpectroMag system from Oxford Instruments. The magnetic field is generated by a
197 superconducting coil with controllable electric current, and the temperature can be controlled by
198 adjusting the heater power to balance with the liquid helium cooling circulation. Four terahertz (THz)
199 transparent windows are embedded in the system for spectrum characterization. A fixed magnetic field
200 direction is aligned to be along two opposite windows and allows for both Faraday and Voigt
201 configuration. A fiber based THz time-domain spectroscopy (TDS) system is used for the terahertz
202 reflection measurement and the THz antennas can be freely arranged to fit with the experimental
203 configuration. The THz beam from transmitter antenna was focused onto the sample with a THz lens
204 and the reflected wave was collected and delivered to the receiver antenna with another lens in the
205 tilted incidence configuration. For the normal incidence case, a 50/50 beam splitter is arranged to
206 redirect the reflected THz wave. The THz beam width is around 5-8mm at the sample surface and the
207 sample size is 15mm×15mm.

208

209 For the THz TDS measurement, both the sample and reference signals are acquired. The reflection
210 signal of samples at room temperature $T=300\text{K}$ is taken as the reference, with InSb acting as metal for
211 THz wave to achieve total reflection of incident THz wave. A time delay range of 100ps after the main
212 THz pulse is scanned for both the sample and reference signals, which corresponds to a frequency
213 resolution of 10GHz. The Fourier-transformed signal of sample is normalized with the reference to
214 give the reflection spectrum. During the measurement, the magnetic field is scanned with a step size of
215 0.01Tesla, so that the reflection spectra on f - B plane can be obtained. In order to reduce the effect of
216 Fabry-Perot resonance between top and bottom surface of InSb, the measured sample ($h=625\text{ }\mu\text{m}$) is
217 attached with another bare InSb substrate (cut from the same InSb wafer) at the bottom to achieve a
218 sample thickness of $h=1250\text{ }\mu\text{m}$, as described in the main text.

219

220 The simulation is carried out with the ‘frequency domain solver’ module of the commercial software

CST microwave studio. In the simulation, the InSb substrate is modeled as gyrotropic dispersion material.

Data Availability

The data that support the findings of this study are available from the corresponding authors upon reasonable request.

Acknowledgement

We thank Zhenwei Zhang and Cunlin Zhang at Capital Normal University for experiment instrument support. This work is supported by the European Research Council Consolidator Grant (TOPOLOGICAL), Horizon 2020 Action Project grant 734578 (D-SPA) and 777714 (NOCTORNO), EPSRC GrantNo. EP/J018473/1, and the National Science Foundation of China (Grant Nos. 61875150 and 61420106006). S.Z. acknowledges support from the Royal Society and Wolfson Foundation. M. N.-C. acknowledges support from University of Birmingham (Birmingham Fellowship), EPSRC (grant No. EP/S018395/1) and the Royal Society (grant No. IES/R3/183131).

Author Contributions

D.W., B.Y. and S.Z. initiated the project and designed the experiment. D.W., Q.Y., X.C., M.W. and J.H. fabricated samples. D.W. and J.H. carried out the measurement. D.W., B.Y., J.H., W.Z. and S.Z. analyzed data. D.W., B.Y., W.G., H.J., M.N.-C. and C.L. performed simulations. D.W., B.Y., W.G., M.N.-C., J.H., W.Z. and S.Z. provided the theoretical explanations. J.H., W.Z. and S.Z. supervised the project. All authors discussed the results and contributed to the final manuscript.

Figure captions:

Figure 1 | Bulk states of lossless magnetized InSb. **a**, The band structure and Weyl points in magnetized plasma system. The parameters used in the calculation are: $\omega_p/2\pi = 0.31$ THz, $B = 0.19$ T and no damping is considered. **b**, Band projection around the outer Weyl point, whose coordinate is $(k_x, k_y, k_z) = (0, 0, 10.8) k_p$ with k_p indicating the vacuum wave vector at plasma frequency. **c**, Band structure with k_z been substituted by B . A fixed value of $k_z = 10.8 k_p$ is assumed and the magnetic field scanning range is $0 \leq B \leq 1$ T. **d**, Dispersion along B around the outer Weyl point in **c**. **e**, Similar to **d** but along $k_{x(y)}$. k_0 indicates vacuum wave vector.

Figure 2 | Observation of terahertz Weyl point in a magnetized semiconductor system. **a**, Schematic of the sample with metal grating on top of the InSb substrate. The specified magnetic field direction is along grating, geometric parameters are: $p = 90$ μm , $h = 1250$ μm and $t = 1$ μm . **b**, Illustration of the experiment setup for terahertz reflection measurement. Two terahertz antennas are placed to be right angle and form a normal incidence onto the sample. ‘BS’ indicates the 50/50 beam splitter. The sample is placed in a commercial equipment with low temperature environment, where the built in superconducting coils provide tunable magnetic field strength. Linear polarization of incidence wave is indicated. **c**, Experimentally measured reflection spectra. The band crossing coordinate can be estimated as $\omega_p/2\pi \approx 0.31$ THz and $B = 0.19$ T. **d**, Reflection spectra calculated with full wave simulation, a damping factor of $\gamma/2\pi = 3 \times 10^{10}$ Hz is considered in the simulation. Red/blue curves are the bulk states and black curves are surface states under lossless assumption, respectively.

Figure 3 | Surface states under tilted incidence excitation. **a**, Schematic experiment configuration with respect of $\theta=45^\circ$ and $\alpha=45^\circ$. The rotation angle of grating is φ about x -axis. $\pm 1^{\text{st}}$ grating order momentum is coupled with incidence wave and excites surface states for corresponding grating angle φ . The material parameters for the sample are $\omega_p/2\pi \approx 0.31$ THz and $\gamma/2\pi = 3 \times 10^{10}$ Hz. **b**, Projected Weyl points on the sample surface plane. **c**, $\pm 1^{\text{st}}$ grating order excited bulk bands within the range of k_x

271 $\in [-100k_0, 100k_0]$ ($+1^{\text{st}}$ bands are indicated with navy color and -1^{st} with purple) and surface states for
 272 $\varphi = 30^\circ$ on the B - f plane. Here we set $\gamma = 0$. **d**, Simulated reflection spectra for $\varphi = 30^\circ$, $h=10\text{mm}$, as
 273 well as the calculated surface states (black dashed) under $\pm 1^{\text{st}}$ grating order excitation. **e**,
 274 Experimentally measured reflection spectra for $\varphi = 30^\circ$, $h=1250\text{ }\mu\text{m}$. **f-h**, Similar to **c-e** but for $\varphi = 45^\circ$.
 275

276 **Figure 4 | Photonic Weyl points and Fermi-arcs in the synthetic space.** **a**, Projected band along k_x
 277 axis on the f - B plane, within the range of $k_x \in [-100k_0, 100k_0]$ for $\varphi=0^\circ$, the Weyl point can be found
 278 around $B=0.472\text{ T}$. **b**, The linear dispersion along φ . **c**, $\pm 1^{\text{st}}$ order grating selected surface state on B - f
 279 plane for $\varphi=-30^\circ$, -45° , -60° . **d**, Similar to **c** but for $\varphi=30^\circ$, 45° , 60° . **e**, Constructed photonic
 280 Fermi-arcs on (B, φ) space for frequency of $f=0.46\text{ THz}$, within the range of $k_x \in [-100k_0, 100k_0]$. **f**,
 281 Similar to **e** but for $f=0.6\text{ THz}$. Cyan hollow dots indicate experimentally measured results.
 282

283 **References:**

- 284 1 Wan, X., Turner, A. M., Vishwanath, A. & Savrasov, S. Y. Topological semimetal and Fermi-arc surface states in
285 the electronic structure of pyrochlore iridates. *Physical Review B* **83**, 205101 (2011).
- 286 2 Burkov, A. A. & Balents, L. Weyl Semimetal in a Topological Insulator Multilayer. *Physical Review Letters* **107**,
287 127205 (2011).
- 288 3 Xu, G., Weng, H., Wang, Z., Dai, X. & Fang, Z. Chern Semimetal and the Quantized Anomalous Hall Effect in
289 HgCr₂Se₄. *Physical Review Letters* **107**, 186806 (2011).
- 290 4 Lu, L., Fu, L., Joannopoulos, J. D. & Soljačić, M. Weyl points and line nodes in gyroid photonic crystals. *Nature*
291 *Photonics* **7**, 294-299 (2013).
- 292 5 Xu, S.-Y. *et al.* Discovery of a Weyl fermion semimetal and topological Fermi arcs. *Science* **349**, 613-617 (2015).
- 293 6 Weng, H., Fang, C., Fang, Z., Bernevig, B. A. & Dai, X. Weyl Semimetal Phase in Noncentrosymmetric
294 Transition-Metal Monophosphides. *Physical Review X* **5**, 011029 (2015).
- 295 7 Lu, L. *et al.* Experimental observation of Weyl points. *Science* **349**, 622-624 (2015).
- 296 8 Soluyanov, A. A. *et al.* Type-II Weyl semimetals. *Nature* **527**, 495-498 (2015).
- 297 9 Huang, L. *et al.* Spectroscopic evidence for a type II Weyl semimetallic state in MoTe₂. *Nature Materials* **15**,
298 1155-1160 (2016).
- 299 10 Lin, Q., Xiao, M., Yuan, L. & Fan, S. Photonic Weyl point in a two-dimensional resonator lattice with a synthetic
300 frequency dimension. *Nature Communications* **7**, 13731 (2016).
- 301 11 Chang, G. *et al.* Room-temperature magnetic topological Weyl fermion and nodal line semimetal states in
302 half-metallic Heusler Co₂TiX (X=Si, Ge, or Sn). *Scientific Reports* **6**, 38839 (2016).
- 303 12 Wang, Z. *et al.* Time-Reversal-Breaking Weyl Fermions in Magnetic Heusler Alloys. *Physical Review Letters* **117**,
304 236401 (2016).
- 305 13 Kübler, J. & Felser, C. Weyl points in the ferromagnetic Heusler compound Co₂MnAl. *EPL (Europhysics Letters)*
306 **114**, 47005 (2016).
- 307 14 Wang, Q., Xiao, M., Liu, H., Zhu, S. & Chan, C. T. Optical Interface States Protected by Synthetic Weyl Points.
308 *Physical Review X* **7**, 031032 (2017).
- 309 15 N.P. Armitage, E. J. M., Ashvin Vishwanath. Weyl and Dirac semimetals in three-dimensional solids. *Reviews of*
310 *Modern Physics* **90**, 015001 (2018).
- 311 16 Ozawa, T. *et al.* Topological photonics. *Reviews of Modern Physics* **91**, 015006 (2019).
- 312 17 Borisenko, S. *et al.* Time-Reversal Symmetry Breaking Type-II Weyl State in YbMnBi₂. Preprint at
313 <https://arxiv.org/abs/1507.04847> (2015).
- 314 18 Liu, E. *et al.* Giant anomalous Hall effect in a ferromagnetic kagome-lattice semimetal. *Nature Physics* **14**,
315 1125-1131 (2018).
- 316 19 Gao, W. *et al.* Photonic Weyl degeneracies in magnetized plasma. *Nature Communications* **7**, 12435 (2016).
- 317 20 Cheng, X. *et al.* Robust reconfigurable electromagnetic pathways within a photonic topological insulator.
318 *Nature Materials* **15**, 542-548 (2016).
- 319 21 Tan, W., Chen, L., Ji, X. & Lin, H.-Q. Photonic simulation of topological superconductor edge state and
320 zero-energy mode at a vortex. *Scientific Reports* **4**, 7381 (2014).
- 321 22 Jin, D. *et al.* Topological magnetoplasmon. *Nature Communications* **7**, 13486 (2016).
- 322 23 Goi, E., Yue, Z., Cumming, B. P. & Gu, M. Observation of Type I Photonic Weyl Points in Optical Frequencies.
323 *Laser & Photonics Reviews* **12**, 1700271 (2018).

324 24 Chen, W.-J., Xiao, M. & Chan, C. T. Photonic crystals possessing multiple Weyl points and the experimental
325 observation of robust surface states. *Nature Communications* **7**, 13038 (2016).

326 25 Yang, B. *et al.* Direct observation of topological surface-state arcs in photonic metamaterials. *Nature*
327 *Communications* **8**, 97 (2017).

328 26 Yang, B. *et al.* Ideal Weyl points and helicoid surface states in artificial photonic crystal structures. *Science* **359**,
329 1013-1016 (2018).

330 27 Noh, J. *et al.* Experimental observation of optical Weyl points and Fermi arc-like surface states. *Nature Physics*
331 **13**, 611-617 (2017).

332 28 O'Brien, T. E., Diez, M. & Beenakker, C. W. J. Magnetic Breakdown and Klein Tunneling in a Type-II Weyl
333 Semimetal. *Physical Review Letters* **116**, 236401 (2016).

334 29 Liu, C.-X., Ye, P. & Qi, X.-L. Chiral gauge field and axial anomaly in a Weyl semimetal. *Physical Review B* **87**,
335 235306 (2013).

336 30 Kharzeev, D. E., Kikuchi, Y., Meyer, R. & Tanizaki, Y. Giant photocurrent in asymmetric Weyl semimetals from the
337 helical magnetic effect. *Physical Review B* **98**, 014305 (2018).

338 31 Yang, Z. *et al.* Weyl points in a magnetic tetrahedral photonic crystal. *Opt. Express* **25**, 15772-15777 (2017).

339 32 Wang, Z., Chong, Y., Joannopoulos, J. D. & Soljačić, M. Observation of unidirectional backscattering-immune
340 topological electromagnetic states. *Nature* **461**, 772-775 (2009).

341 33 Poo, Y., Wu, R.-x., Lin, Z., Yang, Y. & Chan, C. T. Experimental Realization of Self-Guiding Unidirectional
342 Electromagnetic Edge States. *Physical Review Letters* **106**, 093903 (2011).

343 34 Morozov, A. I. *Introduction to Plasma Dynamics*. (CRC Press, Boca Raton, 2012).

344 35 Zhang, S., Xiong, Y., Bartal, G., Yin, X. & Zhang, X. Magnetized Plasma for Reconfigurable Subdiffraction Imaging.
345 *Physical Review Letters* **106**, 243901 (2011).

346 36 Yang, B., Lawrence, M., Gao, W., Guo, Q. & Zhang, S. One-way helical electromagnetic wave propagation
347 supported by magnetized plasma. *Scientific Reports* **6**, 21461 (2016).

348 37 Gangaraj, S. A. H. & Monticone, F. Topological waveguiding near an exceptional point: defect-immune,
349 slow-light, and loss-immune propagation. *Physical review letters* **121**, 093901 (2018).

350 38 Hassani Gangaraj, S. A. *et al.* Unidirectional and diffractionless surface plasmon polaritons on
351 three-dimensional nonreciprocal plasmonic platforms. *Physical Review B* **99**, 245414 (2019).

352 39 Howells, S. C. & Schlie, L. A. Transient terahertz reflection spectroscopy of undoped InSb from 0.1 to 1.1 THz.
353 *Applied Physics Letters* **69**, 550-552 (1996).

354 40 Wang, X., Belyanin, A. A., Crooker, S. A., Mittleman, D. M. & Kono, J. Interference-induced terahertz
355 transparency in a semiconductor magneto-plasma. *Nature Physics* **6**, 126-130 (2009).

356 41 Zhang, Q. *et al.* Superradiant decay of cyclotron resonance of two-dimensional electron gases. *Physical review*
357 *letters* **113**, 047601 (2014).

358 42 Buddhiraju, S. *et al.* Absence of unidirectionally propagating surface plasmon-polaritons in nonreciprocal
359 plasmonics. Preprint at <https://arxiv.org/abs/1809.05100> (2018).

360 43 Hassani Gangaraj, S. A. & Monticone, F. Do Truly Unidirectional Surface Plasmon-Polaritons Exist? , Preprint at
361 <https://arxiv.org/abs/1904.08392> (2019).

362 44 Jia, H. *et al.* Observation of chiral zero mode in inhomogeneous three-dimensional Weyl metamaterials. *Science*
363 **363**, 148-151 (2019).

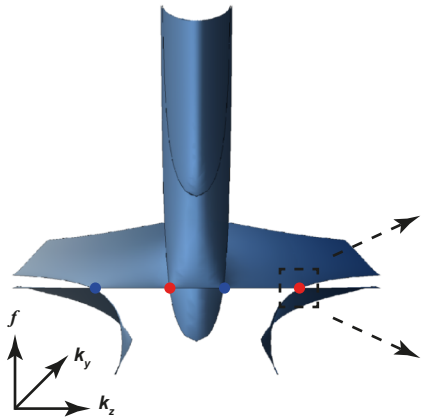
364 45 Gooth, J. *et al.* Experimental signatures of the mixed axial-gravitational anomaly in the Weyl semimetal NbP.
365 *Nature* **547**, 324-327 (2017).

366

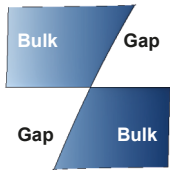
367

368

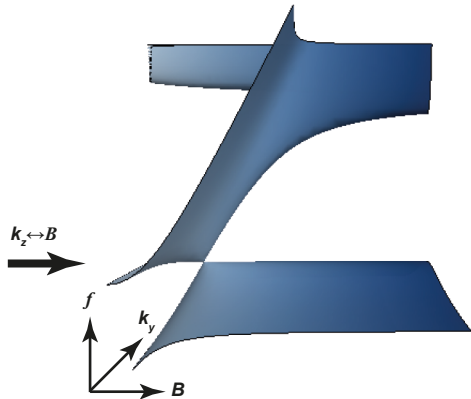
a



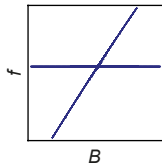
b



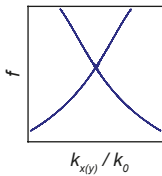
c

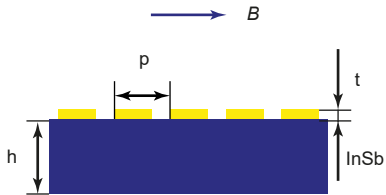
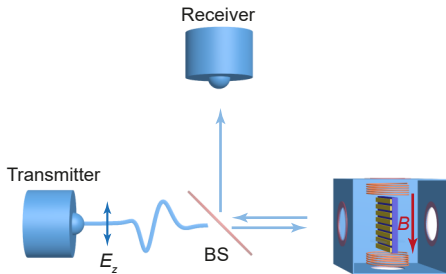
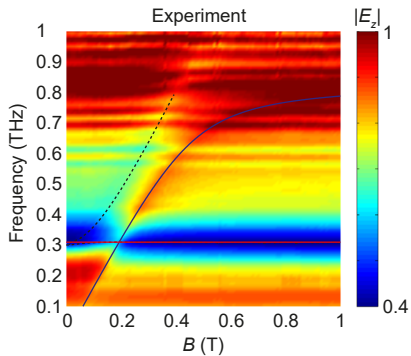
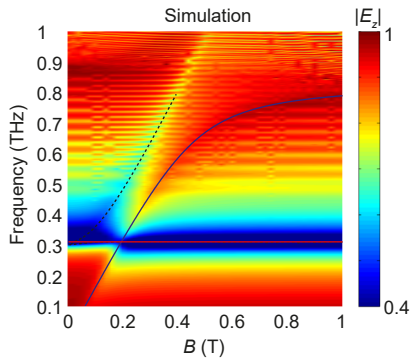


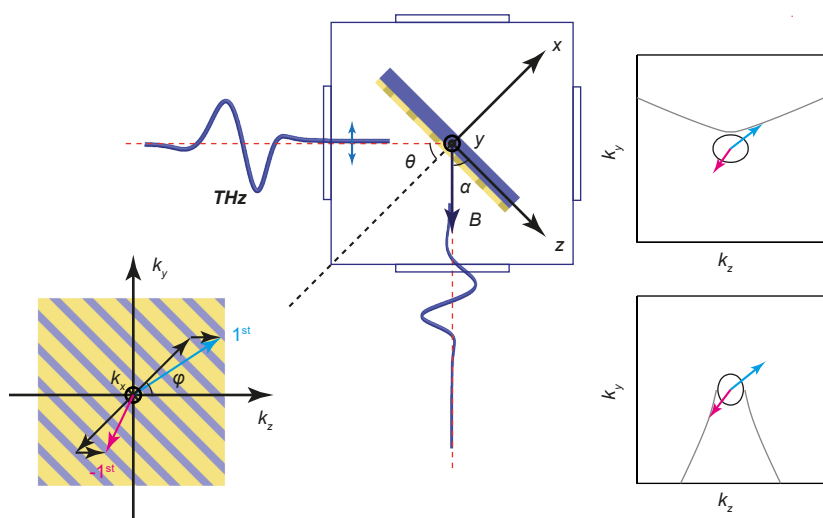
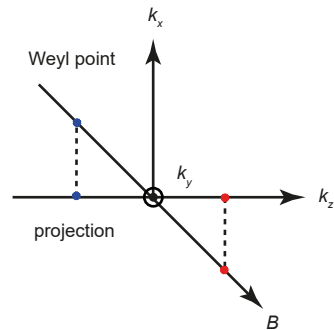
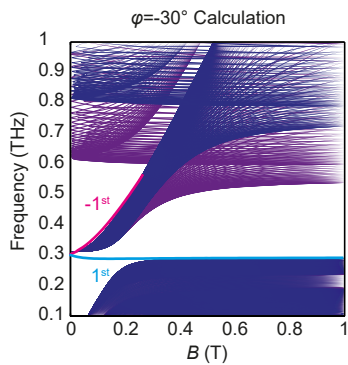
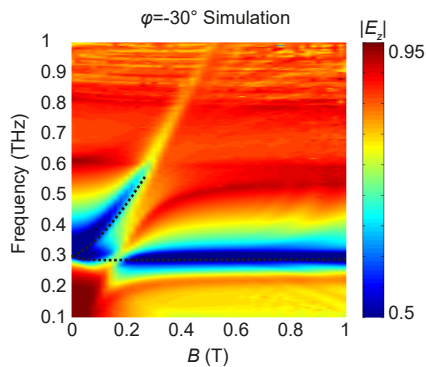
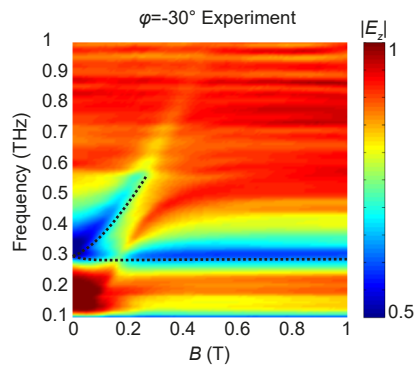
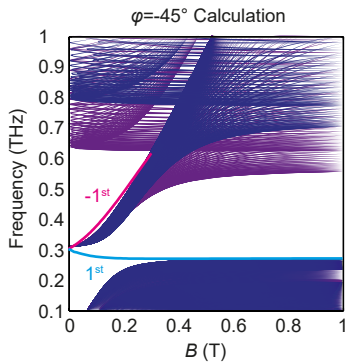
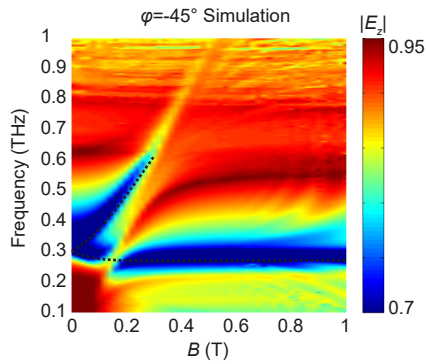
d



e



a**b****c****d**

a**b****c****d****e****f****g****h**